



HAL
open science

A route to an all direct laser written integrated FTS (SWIFTS) in the 3.39–4.1 μm range

Myriam Bonduelle, Guillermo Martin, Alain Morand, Javier R Vázquez de Aldana, Víctor Arroyo Heras, Carolina Romero

► **To cite this version:**

Myriam Bonduelle, Guillermo Martin, Alain Morand, Javier R Vázquez de Aldana, Víctor Arroyo Heras, et al.. A route to an all direct laser written integrated FTS (SWIFTS) in the 3.39–4.1 μm range. *APL Photonics*, 2024, 9 (10), pp.101302. 10.1063/5.0221394 . hal-04837066

HAL Id: hal-04837066

<https://hal.science/hal-04837066v1>

Submitted on 13 Dec 2024

HAL is a multi-disciplinary open access archive for the deposit and dissemination of scientific research documents, whether they are published or not. The documents may come from teaching and research institutions in France or abroad, or from public or private research centers.

L'archive ouverte pluridisciplinaire **HAL**, est destinée au dépôt et à la diffusion de documents scientifiques de niveau recherche, publiés ou non, émanant des établissements d'enseignement et de recherche français ou étrangers, des laboratoires publics ou privés.









Distributed under a Creative Commons Attribution - NonCommercial - NoDerivatives 4.0 International License

LETTER | OCTOBER 14 2024

A route to an all direct laser written integrated FTS (SWIFTS) in the 3.39–4.1 μm range

Special Collection: [Mid-IR Photonics](#)

Myriam Bonduelle ; Guillermo Martín ; Alain Morand ; Javier R. Vázquez de Aldana ; Víctor Arroyo Heras ; Carolina Romero 



APL Photonics 9, 101302 (2024)
<https://doi.org/10.1063/5.0221394>



Articles You May Be Interested In

Light interference detection on-chip by integrated SNSPD counters

AIP Advances (October 2011)

Fluorescence imaging of lattice re-distribution on step-index direct laser written Nd:YAG waveguide lasers

J. Appl. Phys. (January 2015)

Creating large second-order optical nonlinearity in optical waveguides written by femtosecond laser pulses in boro-aluminosilicate glass

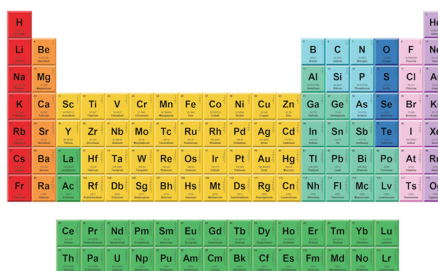
Appl. Phys. Lett. (January 2014)

06 December 2024 15:34:54



THE MATERIALS SCIENCE MANUFACTURER®

Now Invent.™



American Elements
 Opens a World of Possibilities

...Now Invent!

www.americanelements.com

© 2021-2024 American Elements & U.S. Registered Trademark

A route to an all direct laser written integrated FTS (SWIFTS) in the 3.39–4.1 μm range

Cite as: APL Photon. 9, 101302 (2024); doi: 10.1063/5.0221394

Submitted: 31 May 2024 • Accepted: 23 September 2024 •

Published Online: 14 October 2024



View Online



Export Citation



CrossMark

Myriam Bonduelle,^{1,a)} Guillermo Martin,¹ Alain Morand,² Javier R. Vázquez de Aldana,³
Víctor Arroyo Heras,³ and Carolina Romero³

AFFILIATIONS

¹ Univ. Grenoble Alpes, CNRS, IPAG, 38000 Grenoble, France

² Univ. Grenoble Alpes, Univ. Savoie Mont Blanc, CNRS, Grenoble INP Institute of Engineering Univ. Grenoble Alpes, CROMA, 38000 Grenoble, France

³ Grupo de Investigación en Aplicaciones del Láser y Fotónica (ALF-USAL), Facultad de Ciencias, Universidad de Salamanca, E-37008 Salamanca, Spain

Note: This paper is part of the APL Photonics Special Topic on Mid-IR Photonics.

^{a)} **Author to whom correspondence should be addressed:** myriam.bonduelle@univ-grenoble-alpes.fr

ABSTRACT

This work aims to present the building blocks for an all direct laser written integrated spectrometer in the mid-infrared (3.39–4.1 μm range) based on the SWIFTS (Stationary Wave Integrated Fourier Transform Spectrometer) principle. In a SWIFTS-Gabor configuration, the light from the source interferes with itself in the middle of a channel waveguide, creating a stationary wave. This interferogram is then sampled through scattering centers placed on top of the waveguide that radiate the light they extract onto a detector placed directly on the sample. Finally, the spectrum of the source is retrieved through a Fourier transform. To implement a SWIFTS, two main photonic functions are required: the waveguide and the scattering centers. In this work, both functions have been created using Direct Laser Writing (DLW), a versatile technique, allowing to easily access 3D configurations and to reduce fabrication time. DLW focuses a femtosecond laser onto a sample so as to locally change the crystal lattice, resulting in its structural modification. The waveguides presented here are surface half-circular cladding structures made through type II modifications in the sample, and the scattering centers are surface damage tracks (also referred to as grooves). These surface tracks are creating dielectric discontinuities in the evanescent part of the stationary wave, resulting in the light being radiated outside the waveguide. All of these are made in a z-cut lithium niobate substrate for future implementation of the electro-optic effect. We demonstrate that we have functional waveguides in the mid-IR and that our grooves are extracting the stationary wave as expected, showing promising results for future implementation of a complete mid-IR SWIFTS using DLW.

© 2024 Author(s). All article content, except where otherwise noted, is licensed under a Creative Commons Attribution-NonCommercial-NoDerivs 4.0 International (CC BY-NC-ND) license (<https://creativecommons.org/licenses/by-nc-nd/4.0/>). <https://doi.org/10.1063/5.0221394>

I. INTRODUCTION

A. Context

A spectrometer is an instrument that allows the quantitative spectral analysis of an incident light signal, with great potential in the study of the composition of a material or medium based on its response to a given wavelength range (excitation source). Spectrometers are used in multiple domains, such as astrophysics,¹ environmental monitoring,² biosciences (in particular medicine),³ or material sciences.⁴ Traditional spectrometers offer unparalleled resolution over wide spectral ranges. For example, the CRIRES/VLT

instrument has a resolution of $R = 100\,000$ and a spectral range of 0.92–5.3 μm , as compared to the expected performances of a mid-IR Stationary Wave Integrated Fourier Transform Spectrometer (SWIFTS), around $R = 10\,000$ (corresponding to a resolution of 340 pm) over a range of a few dozens of nanometers. However, traditional spectrometers are usually characterized by numerous and bulky relay optics and are thus voluminous and costly instruments. CRIRES/VLT is a few meters high and wide,¹ whereas a complete SWIFTS is only a few centimeters large. Newer applications (satellite monitoring, space missions, *in situ* measurements. . .) are calling for smaller, more cost-efficient spectrometers, paving the

way to the development of miniature integrated spectrometers.⁵ In the visible and near-infrared range, such spectrometers have been demonstrated, with sizes in the millimeter range and resolutions of a few nanometers over ranges of a few hundred nanometers.^{6–8} However, the extreme reduction of the footprint comes with repeatability issues, higher fabrication costs, and lower resolutions. Depending on the desired application, either of these characteristics may be more interesting than the others, leading to the need to further develop miniature spectrometers tailored for different applications: higher resolution—possibly also increasing the footprint, longer wavelengths, lower costs. . . .⁹

In the mid-infrared (MIR $2.5\ \mu\text{m}$ to $25\ \mu\text{m}$) range, miniature spectrometers have also been demonstrated,^{10–12} with a resolution of a few hundred nm over a wide wavelength range ($400\ \text{nm}$ over $1\text{--}9.5\ \mu\text{m}$ or $90\ \text{nm}$ over $4\text{--}7\ \mu\text{m}$ ¹¹) or a few nm over a smaller range ($3\ \text{nm}$ over $300\ \text{nm}$ ¹²), but even higher resolution spectrometers are still lacking in this wavelength range.¹³ Such mid-infrared miniature spectrometers are easily transportable, making them very useful for *in situ* measurements. They could find their application in a wide variety of domains, such as gas sensing applications, where the requirements are for a resolution of $1\text{--}5\ \text{nm}$ at $5\ \mu\text{m}$,¹⁴ in the medical field (possible leukemia tracer through the measurements of lipid concentration¹⁵). . . . In parallel, integrated Fourier Transform Spectrometers (FTS) are showing promising results when it comes to ultra-high resolution: $0.47\ \text{nm}$ at $1.55\ \mu\text{m}$,¹⁶ or, more recently, $0.16\ \text{nm}$ at $1.55\ \mu\text{m}$ with a silicon base temporal heterodyne FTS.¹⁷ In particular, the SWIFTS¹⁸ design has attained very high resolution in the visible range ($0.16\ \text{nm}$ at $635\ \text{nm}$ ¹⁹) and up to $5\ \text{pm}$ in the $630\text{--}1000\ \text{nm}$ in its commercial version.²⁰ Newer results in the near infrared ($1.55\ \mu\text{m}$) led to resolutions of a few nm (5.5 and then $1.2\ \text{nm}$),^{21,22} although in this case without an integrated detector.

In view of these results, we are presenting here the building blocks (waveguides and scattering centers) to implement a miniature integrated spectrometer around $3.4\ \mu\text{m}$ (mid-infrared) in a Gabor configuration. As the expected resolution of a mid-IR SWIFTS is below $1\ \text{nm}$, such an instrument could be an interesting step toward very high resolution MIR spectrometers. Additionally, the technology used to fabricate our samples is Direct Laser Writing (DLW), a rapid and, therefore, cost-effective technology. It is also versatile, with the possibility to write 3D configuration, to easily change the designs and parameters of the photonic functions, and to implement all the required building blocks in a single technological run. Finally, the choice of the material (lithium niobate) was guided by the future implementation of the electro-optic effect so as to obtain active phase modulation in the spectrometer.

B. SWIFTS principle

In a Gabor configuration, a stationary wave is obtained by injecting the light from the source on both sides of a channel waveguide. Dielectric discontinuities (in our case, grooves created by ablating the surface of the material) are placed on top of the waveguide, allowing to sample the interferogram created by the propagative and counter-propagative waves interfering with one another. The resulting stationary interferogram is radiated by the discontinuities onto a detector, placed directly on top of the waveguide, allowing to avoid any relay optics. Finally, the spectrum of the source is retrieved through a Fourier transform.

To reduce the angular divergence of the radiation pattern of the grooves, which, in the case of a large substrate layer in the detector, may result in crosstalk (leakage of the signal from one pixel onto the neighboring pixels, leading to an impossibility to reconstruct the signal), several grooves per scattering center (hereafter referred to as antennas) have been implemented.²³ An antenna based on multiple grooves emitting light with coherent phase can be seen as a miniature diffraction grating, allowing for a reduction of the angular divergence of the diffracted flux (Fig. 1) and for more flux to be extracted, thus increasing the SNR (Signal-to-Noise Ratio).

C. SWIFTS characteristics

In a SWIFTS Gabor, for a waveguide of length L along the x axis, with $x = 0$ at the center of the waveguide, the total optical field resulting from the addition of the propagative and contra-propagative waves can be expressed as

$$\vec{E}_T = \vec{E}_0 \cdot e^{i \frac{2\pi}{\lambda} n_{eff} (\frac{-L}{2} + x)} + \vec{E}_0 \cdot e^{-i \frac{2\pi}{\lambda} n_{eff} (\frac{L}{2} + x)}, \tag{1}$$

where n_{eff} is the effective index of the fundamental guided mode in the waveguide and x is the position along the propagation direction. The electric fields described in Eq. (1) are λ/n_{eff} periodic. In order to sample the interferogram at an equivalent phase so as to radiate the signal vertically, the required pitch between two consecutive grooves in an antenna (pitch of the grating) is $\Lambda = \frac{\lambda}{n_{eff}}$, corresponding in our situation to $\Lambda \sim 1.6\ \mu\text{m}$ (Fig. 2).

Theoretically, the pitch between two consecutive antennas should respect the Shannon–Nyquist criteria for the sampling of the interferogram, meaning that we should have $p = \frac{\lambda}{4n}$.¹⁸ However, in practice, the pitch between the antennas p is limited by the usual pixel pitch in mid-infrared detectors: an antenna pitch p smaller than the classical pitch size will result in crosstalk (Fig. 1). Assuming this limitation, the fundamental equations that will describe the performances of the SWIFTS are given.¹⁸

The spectral resolution of a SWIFTS is

$$R = \frac{\lambda}{\delta\lambda} = \frac{2 \cdot n_{eff} \cdot L}{\lambda}, \tag{2}$$

and its useful spectral bandwidth,

$$\Delta\lambda = \frac{\lambda^2}{4 \cdot n_{eff} \cdot p}. \tag{3}$$

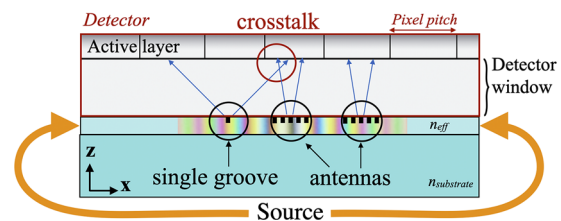


FIG. 1. Principle of a SWIFTS Gabor: the light is injected on both sides of the waveguide, creating an interferogram with an optical path difference of 0 in the middle of the waveguide. This interferogram is extracted by the scattering centers, grooves, arranged in an antenna configuration onto a detector placed directly on top of the waveguide.

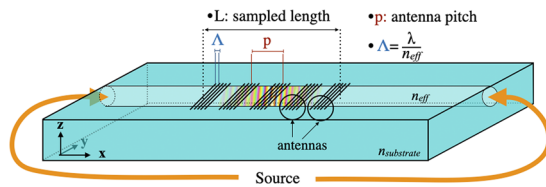


FIG. 2. Characteristics of a SWIFTS: L is the total sampled length, p the pitch between the antennas, Λ the grating pitch, i.e., the pitch between two grooves, and n_{eff} the effective refractive index of the waveguide.

With these equations, a mid-infrared SWIFTS ($\lambda = 3.39 \mu\text{m}$), with a sampled length of $L = 1 \text{ cm}$, will have $R > 10\,000$, i.e., the minimum wavelength separation distinguishable $\delta\lambda \approx 340 \text{ pm}$. Additionally, for a classical pixel pitch of $p = 30 \mu\text{m}$ in commercial mid-IR detectors, we will have $\Delta\lambda \sim 44 \text{ nm}$. Finally, the number of pixels on the detector will also determine the maximum length (L) that can be sampled (corresponding to the size of the detector).

Although the SWIFTS is a high resolution spectrometer (notably in regard to its size), the spectral bandwidth is quite limited, mainly due to the high pixel pitch in commercial mid-IR detectors. To increase the achievable bandwidth, several solutions can be implemented, such as spatial multiplexing, consisting of several waveguides injected simultaneously,²⁴ or temporal multiplexing, a temporal modulation of the phase through the use of different techniques locally modifying the refractive index of the material. This will allow us to scan the interferogram under the sampling centers, thus virtually reducing the spacing between consecutive data, as if the distance between antennas were reduced. In the case of lithium niobate, this temporal modulation is achieved through the electro-optic effect.

D. LiNbO₃ samples

Our device was made in z-cut lithium niobate (LiNbO₃) bulks. LiNbO₃ is a bi-refrariant crystal, meaning that it shows different refractive indices depending on the propagation and polarization directions of the light: ordinary index n_o along the x and y axes, and extraordinary index n_e along the z axis. Lithium niobate is relatively transparent in the 3.39–4.1 μm range, with an absorption coefficient $\alpha \sim 0.12 \text{ dB/cm}$,²⁵ and it presents electro-optic (EO) properties. These EO properties mean that the local refractive index can be changed (Δn_{EO}) through the application of an electric field (E), here applied along the y axis, with the following equation:

$$\Delta n_{\text{EO}} \approx \frac{1}{2} n^3 r_{52} E = \frac{1}{2} n^3 r_{51} E. \quad (4)$$

With r_{52} and r_{51} the electro-optic coefficients of LiNbO₃ in the case of an electric field applied along the y axis of the crystal, usually of a few dozens of pm/V. The implementation of the electro-optic effect requires to deposit electrodes and then connectorize them so as to apply an electric field on either side of a chosen waveguide. Preliminary trials to deposit golden electrodes were tested on our sample, although unsuccessfully.

We are currently trying to optimize the procedure, as the electrodes do not seem to stick properly on top of the sample

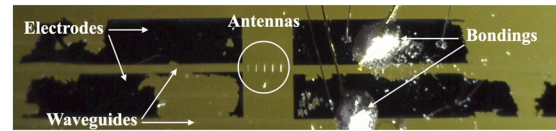


FIG. 3. Preliminary trials for the deposition of gold electrodes (darker squares) on top of the sample. The waveguides can be seen horizontally across the sample, and the antennas vertically in the second waveguide. The wire bondings can also be seen.

(Fig. 3). Even though our preliminary trials did not give any efficient EO modulation, previous work, such as the waveguides implemented by Heinrich *et al.*,²⁶ has shown that it can be implemented in DLW waveguides written in LiNbO₃.

II. FABRICATION

As DLW allows us to create both the waveguides and the (sub)-micron structures required for a complete SWIFTS spectrometer, everything was fabricated using a femtosecond laser by the ALF-USAL group in Salamanca. When focusing a femtosecond laser onto a sample, a very high optical intensity is obtained in the focal plane in the material, resulting in the ionization of a large number of electrons that then break away from their atoms. The interaction of these electrons with the laser pulse eventually leads to the creation of a hot and dense electronic plasma²⁷ which, when breakdown occurs, will result in an energy transfer to the lattice. This irradiation can cause a structural modification of said lattice, resulting in localized permanent changes, such as cracks or even a void.²⁸

In this work, both the waveguides and the grooves were made using an amplified Ti:sapphire femtosecond laser system (Spitfire Ace, Spectra-Physics), delivering 60 fs pulses at a central wavelength of 800 nm and with a repetition rate of 5 kHz. The beam power was controlled by a half-wave plate and a linear polarizer before being focused by a 40 \times microscope objective. The sample was placed in a three-axis motorized micropositioning stage that scans the sample in the focus of the beam at a constant velocity to produce damage tracks (focusing inside the crystal) or ablation grooves (focusing at the crystal surface).

The aforementioned parameters are not changed throughout the fabrication process, but depending on the desired effect (in-depth track for the waveguide or surface damage for the grooves), the remaining parameters (irradiation laser power, scanning speed, or focusing depth) were changed.

A. Waveguides

Direct laser written waveguides using femtosecond lasers were initially demonstrated in glass samples²⁹ before being generalized to other materials, notably lithium niobate.³⁰ In dielectric crystals, creating a waveguide implies a localized modification of the refractive index in the bulk that can be performed in two ways: type I or type II modification,³¹ the latter being the modification implemented in our sample.

In type II modification, the tracks created by the laser have a negative refractive index change ($\Delta n < 0$), due to a localized crystalline lattice expansion in the bulk. This expansion leads in turn to a localized compression of the lattice in the vicin-

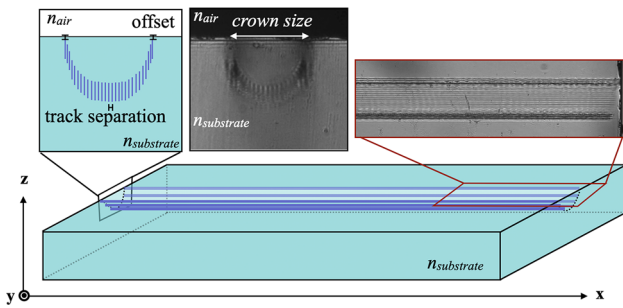


FIG. 4. Schematics (bottom) of z-cut sample, with a waveguide written along the x axis. The crown shape created by the tracks observed on the facet of the sample (left and middle insets) is propagating along the waveguide’s direction. On the right inset (microscope image of the waveguide on the surface of the sample), the tracks can be observed at different depths in the sample: the edges are at the surface, and the lines at the center are inside the sample.

ity of the tracks, this time leading to a higher refractive index. Using this, a waveguide can be created by arranging the tracks in a way that defines a cladding where the refractive index decreases with respect to the bulk; these waveguides are the so-called depressed-index cladding waveguides and were first implemented in a YAG crystal³² and then in lithium niobate.³³ The great advantage of such a fabrication strategy is that any desired size and geometry of the waveguide can be arranged, leading to a rather precise modal control. In this work, a half-circular cladding (half-crown) at the surface of the waveguide was implemented. These tracks are then propagated along the waveguide (Fig. 4). A notable drawback of this type of waveguide is that the limited thickness of the cladding can induce some propagation losses. A part of the signal in the core can leak outside the waveguide along the propagation, increasing the propagation losses (Table I).

The *irradiation power* corresponds to the power effectively arriving onto the surface of the sample; that depends on the energy (in J) of the pulse, their repetition rate, and the transmission ratio of the optics the beam went through. The irradiation power value has been selected after several trials as the optimum value for which damage tracks could be produced at all the required depths in the sample (to complete the waveguide cladding) while avoiding focal distortions and cracking of the sample.

The *scanning speed* describes how long a given location of the sample remains irradiated by the laser. For a given pulse energy, decreasing the scanning speed will result in a more intense modification of the material as it increases the number of pulses incident on each sample point.

TABLE I. Parameters for the waveguide fabrication. Each of them will be described in further details in the text.

Irr. power (mW)	Scanning speed ($\mu\text{m/s}$)	Track separation (μm)	Offset (μm)	Crown size (μm)
0.42	500	2	12	35

The *track separation* in a waveguide corresponds to the distance between two consecutive tracks inside the crystal lattice. This separation dictated the stress induced inside the material, therefore the refractive index change obtained in the waveguide. The separation of $2 \mu\text{m}$ was determined as optimal in the case of DLW LiNbO₃ waveguides.^{34,35}

The *offset* represents the focalization point inside the sample. An offset of $z = 0$ means that the focalization will be performed on the surface of the sample, whereas a positive offset means a focalization inside the sample and a negative one outside. Having no offset may result in ablation at the surface of the sample because of the high energy of the pulses that are irradiating the crystal. However, an offset too big (deep inside the sample) may result in a crown not being closed, therefore leading to a waveguide not properly confining the light.

The *crown size* is crucial to determine the modal behavior range of the waveguide: for a given refractive index change, increasing the diameter of the crown will increase the wavelengths at which the waveguide is monomode, and vice versa. In our case, the crown diameter is $35 \mu\text{m}$, as this size was expected to be monomode in our wavelength range ($3.39\text{--}4.1 \mu\text{m}$). However, this diameter is actually too wide, resulting in a slightly multimode waveguide.

B. Grooves

The grooves were made by ablating the material using the same femtosecond laser. Because the fabrication process of the grooves is ablation, an ultra-sound cleaning bath is required after the processing in order to remove the material particles deposited both on the grooves and on the surface (debris) (Fig. 5).

For the choice of the irradiation parameters, we first fixed the scanning speed to a value that ensures a large overlap between consecutive pulses. Then, we found the minimum power at which a uniform and regular ablation groove was produced. The focusing conditions are very critical, as changes of $1\text{--}2 \mu\text{m}$ in the focal plane lead to the failure of the fabrication process (Table II).

Following the SWIFTS’s characteristics presented in Subsection I C, five antennas were implemented, each with a different number of grooves. The first antenna has 1 groove, the second 3, then 5, 7, and the last antenna has 9 grooves. The separation between two consecutive grooves in an antenna is $1.6 \mu\text{m}$. The waveguide was then injected with a $3.39 \mu\text{m}$ HeNe laser (from one side only), so as to study the diffraction pattern of the antennas (Fig. 6).

III. RESULTS AND DISCUSSION

A. Characteristics of the obtained waveguide

When locally changing the crystalline lattice of a material, propagation losses are expected to be induced. These losses, created by the waveguide, are a defining factor in judging the quality of the aforementioned waveguide, which is why we tried to retrieve

TABLE II. Parameters for the grooves fabrication.

Parameters	Power (mW)	Scanning speed ($\mu\text{m/s}$)	Offset (μm)
Grooves	0.31	50	0

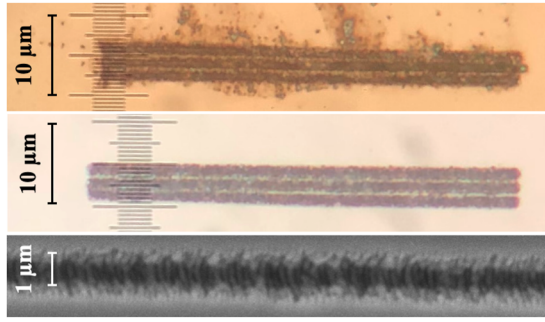


FIG. 5. Optical microscope image of three grooves, separated by 1.2 μm , made by direct laser writing, before (top) and after (middle) an ultra-sound bath. The grooves obtained after the ultra-sound bath were then imaged (bottom) using a scanning electron microscope (SEM).

an estimation of these losses from our measurements. In addition to the overall waveguide quality, these propagation losses will have an impact on the propagating field and, therefore, on the reconstructed spectra. As this impact has to be taken into account during the calibration of the device, these propagation losses need to be quantified. This was performed by injecting the sample with a single-mode mid-infrared fiber and focusing its output onto a mid-IR camera with another converging lens, resulting in an image of its output³⁶ displayed in Fig. 7.

Once the output of the waveguide has been imaged, estimating the value of the absorption coefficient requires to first identify the possible other loss sources (coupling losses, Fresnel reflection...), remove them from the total flux injected, and then compare the result with the output. The coupling losses are induced by the mismatched sizes of the guided modes and the fiber modes and are determined by calculating the overlapping between the fiber mode and the guided mode,

$$T_{\text{coupling}} = \frac{(\iint \sqrt{I_{\text{fiber}}} \sqrt{I_{Wg}} dS)^2}{\iint I_{\text{fiber}} dS \iint I_{Wg} dS}, \quad (5)$$

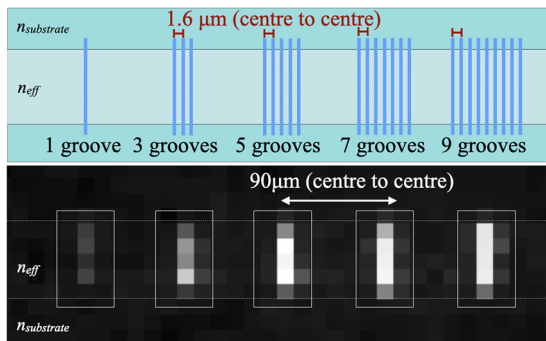


FIG. 6. Schematics (top) and mid-IR radiated field (bottom) of the grooves written on top of the waveguide, as seen by the detector placed perpendicular to the surface. Each antenna is separated by 90 μm , and two consecutive grooves in an antenna are separated by 1.6 μm . The number of grooves per antenna is varying (1, 3, 5, 7, and 9 grooves), resulting in a change in the extracted intensity.

where I_{fiber} and I_{Wg} are the 2D spatial intensity distribution of the fiber and the waveguide, respectively. Finally, the propagation transmission, $T_{\text{propagation}}$ is then deduced from the corrected injected flux and the collected flux at the output of the waveguide. From $T_{\text{propagation}}$, the absorption coefficient α , in dB cm^{-1} , can be retrieved

$$\alpha_{\text{dB cm}^{-1}} = 10 \cdot \log(e) \cdot \frac{-\ln(T_{\text{propagation}})}{L}, \quad (6)$$

with L the length of the waveguide. In our samples, we found $\alpha = 2.19 \text{ dB cm}^{-1}$, which gives the transmission rate in percent of our chip (1 cm long): 60.4%. These results are aligning with previous type II tracks in LiNbO_3 results (an absorption coefficient of 2.9 dB cm^{-1} was obtained by Nguyen³⁵). Depending on the desired application, these losses can be considered rather high, but solutions can be implemented to improve this value: for instance, thermal annealing allowed to obtain losses around 1.5 dB cm^{-1} in similar (LiNbO_3 , type II tracks) waveguides.³⁴

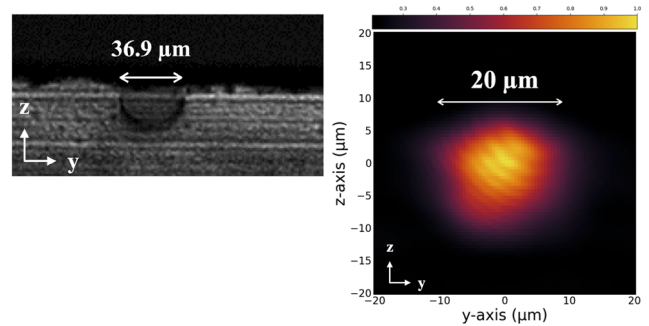


FIG. 7. Output of the waveguide: (top): in white light using an optical microscope, and (right): when the waveguide is injected at 3.39 μm .

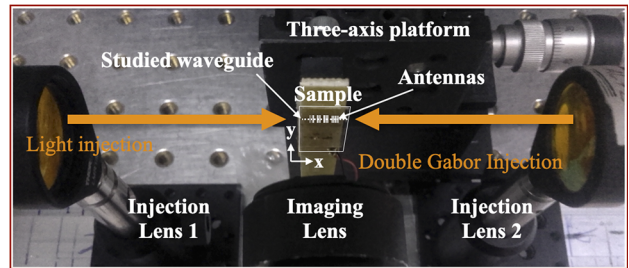
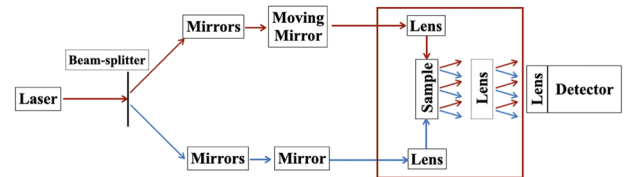


FIG. 8. Image of the optical setup. The flux from a HeNe laser at 3.39 μm is split before being injected on both sides of a waveguide through converging lenses. One of the injection arms is a mirror on a motorized translation axis, allowing to externally change the optical path difference. This creates an interferogram in the middle of the waveguide, which is then extracted by the antennas and imaged onto a detector (in our case, a FLIR camera).

06 December 2024 15:34:54

TABLE III. Obtained contrast for each of the antennas, containing different numbers of grooves.

1 groove	5 grooves	7 grooves	9 grooves
0.26	0.27	0.31	0.37

TABLE IV. Parameters of the grooves for the implementation of numerous antennas.

Parameters	Power (mW)	Scanning speed ($\mu\text{m/s}$)	Offset (μm)
Grooves	0.28	50	1

B. Interferometric response of the antenna

In order to study the oscillation pattern of the antenna, the waveguide was injected in a Gabor like configuration. In a final SWIFTS design, this injection is made through optical fibers, and such an injection setup has been tested using Thorlabs Mid-IR fluoride fibers (in ZrF4). However, to test our building blocks, the optical path difference needed to be externally modulated, requiring a mirror and a ZnSe focusing lens for the injection (Fig. 8).

The light from the source (HeNe 3.39 μm laser) is split into two paths and then injected on each side of the waveguide through converging lenses, with one of the injection arms that can be moved with

respect to the other. Finally, the radiation pattern of the antenna is imaged onto a FLIR with an imaging lens. The FLIR camera, from the SC-7000 series, operates from 1.5 to 5 μm , with an indium antimonide detector (InSb, with a 30 μm pixel pitch), and must be cooled down. In a final mid-IR SWIFTS prototype, such a detector is not adapted due to its size and power consumption and will be replaced by a smaller, uncooled detector. In that regard, developments are currently ongoing using uncooled and uncapped mid-IR detectors from NIT (New Infrared Technologies).

The external modulation is obtained by scanning one of the mirrors set on a motorized translation axis (Physik Instrumente). This allows us to change the optical path difference between the two arms, thus creating an interferogram, described by the following equation:

$$I_T = I_1 + I_2 + 2 \cdot \sqrt{I_1 \cdot I_2} \cdot \cos\left(\frac{2\pi}{\lambda} \cdot \delta\right), \tag{7}$$

with I_1 and I_2 the flux from the two arms of the interferometer, and δ the optical path difference (OPD). The OPD corresponds to the geometrical path difference (GPD) multiplied by the refractive index in which this GPD happens. In particular, in the case of an external modulation (the GPD Δx is changed before being injected in the waveguide), the OPD δ is expressed as $\delta = n_{ext} \cdot \Delta x$. In the case of an internal modulation (use of the EO effect), the OPD is expressed as $\delta = \Delta n_{EO} \cdot L_{EO}$, with Δn_{EO} the index modification given by Eq. (4) and L_{EO} the length of the electrodes used for the EO modulation.

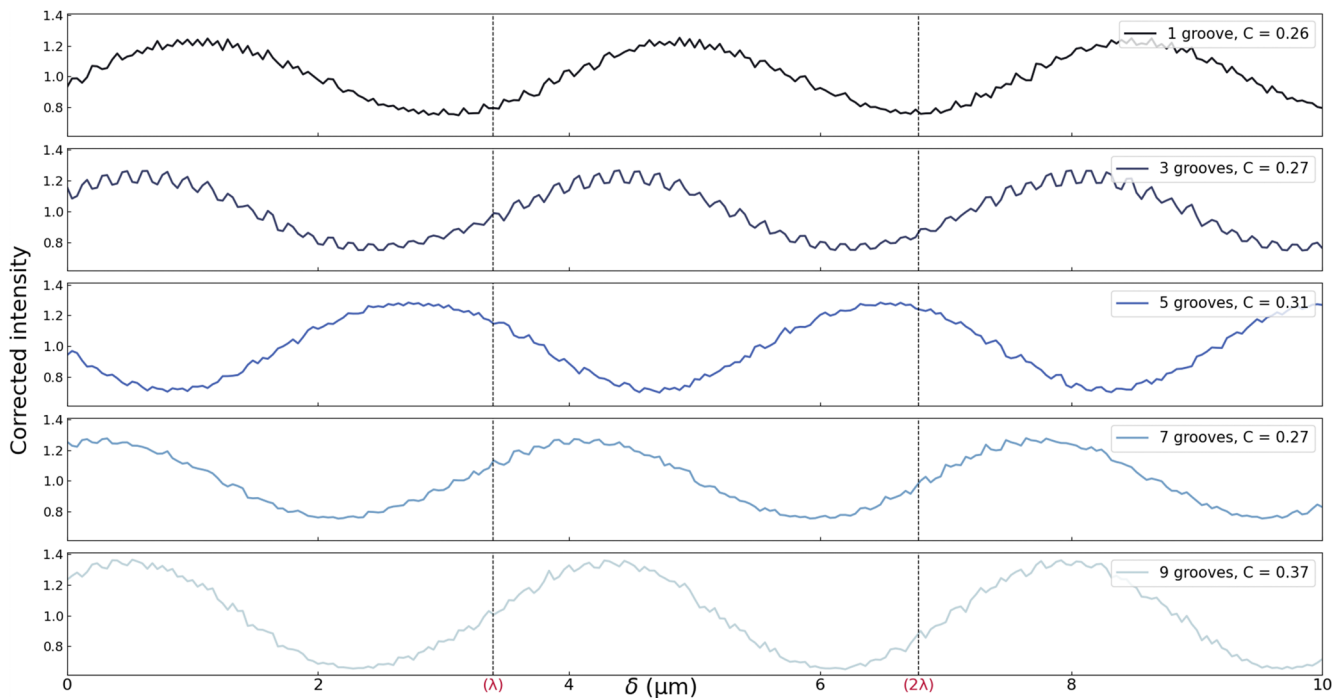


FIG. 9. Flux extracted by each antenna when an interferogram is created in the waveguide by injecting it on both sides with a HeNe laser (3.39 μm) and with the optical path difference (OPD) externally modulated through the use of a motorized translation axis in one of the injection arms. The x axis represents the OPD in μm , and the y axis the corrected extracted intensity [following Eq.(8)]. The contrast for each antenna is added, as well as the expected periodicity (λ).

When externally modulating the optical path difference, the interferogram is expected to have a period of λ , as the cosine function is 2π periodic, and $n_{ext} = n_{air} = 1$. The response of each antenna to this external modulation was then extracted, and the intensity was corrected as expressed in the following equation:

$$I_{corr} = 1 + \frac{I_{T,mes} - (I_1 + I_2)}{2 \cdot \sqrt{I_1 \cdot I_2}}. \quad (8)$$

The corrected intensity was plotted in Fig. 9 so as to study the capacity of the antennas to extract the interference pattern created. The contrast, defined as

$$C = \frac{I_{T,max} - I_{T,min}}{I_{T,max} + I_{T,min}}, \quad (9)$$

is also calculated for each of the groups (see Fig. 9) and found in Table III.

The theoretical maximum value of the contrast is 1, obtained in the case of a perfect balance between the arms of the interferometer ($I_1 = I_2$). Here, the obtained contrast for every antenna is between 20% and 30%. This was expected, as the bench has not been perfectly balanced ($I_1 \neq I_2$ will result in a diminished contrast). However, the oscillation pattern due to the external modulation is observed, meaning that the antennas can sample the interferogram. Additionally, the period of the sampled interferogram is close to the expected period, that is to say λ . The period is not exactly λ , as can be seen in Fig. 9, due to the fact that the optical setup contains a motorized translation axis that is not necessarily entirely smooth in its movement, leading to an imprecise obtained δ that does not necessarily correspond to the theoretical one. As the period between the antennas is not a multiple of the period of the fringes in the waveguide, even if they are regularly spaced, there is no guarantee that the sampling will be made identically. This results in an apparent phase shift between the different antennas.

C. Increasing the number of antennas

In order to improve the resolution of the SWIFTS [Eq. (2)], the sampled length must be as long as possible. To do so, the number of antennas can be increased without extracting too much of the light propagating inside the waveguide. As DLW antennas are quick and easy to fabricate, a sample containing several waveguides, each with a different number of antennas N_a was implemented. The sample is still a z-cut LiNbO₃ sample, and the waveguides are similar to the one previously mentioned (meaning that they are also multimode; Table IV).

Four waveguides were implemented, with $N_a = 5$ antennas, 11 antennas, 21 antennas, 41 antennas, and an additional waveguide not containing any antenna ($N_a = 0$). All of the antennas have the same parameters (5 grooves, separated by $1.6 \mu\text{m}$) and have been imaged when the waveguide is injected from one side only (due to time constraints), considering that the reflection is null [Fig. 10 (top)]. The total intensity extracted when considering all the antennas of a waveguide, which should vary with $I_{tot} = N_a \cdot I_0$, was extracted from the obtained data [Fig. 10 (bottom)].

Figure 10 (bottom) shows that the total extraction from the antenna varies very closely with the number of antennas, as expected, although $N_a = 5$ seems to be rather high compared to its number. It is important to note that it also depends on the quality

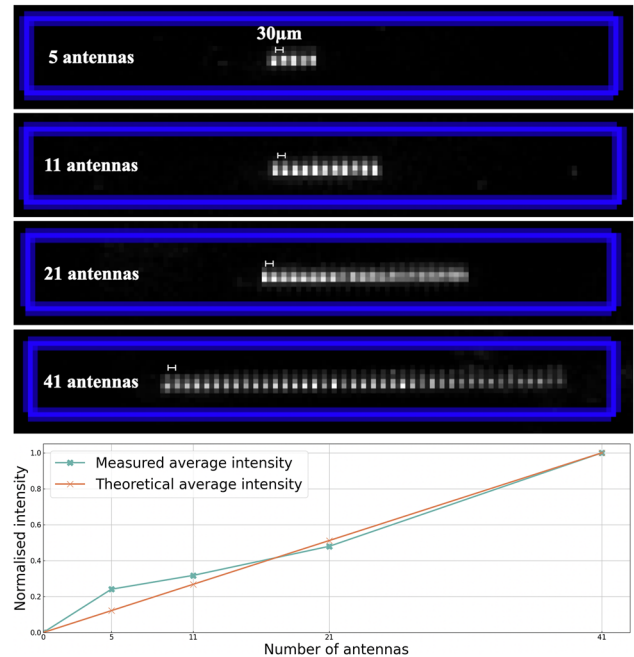


FIG. 10. Top: Image on the pixel matrix of the detector of the radiation pattern of the antennas observed when injecting the waveguides from one side only with a HeNe laser, with $N_a = 5$ on the first waveguide, then $N_a = 11$, $N_a = 21$, and $N_a = 41$. Each of the antennas is composed of five grooves separated by $1.6 \mu\text{m}$, and each antenna is separated by $30 \mu\text{m}$. Bottom: Normalized extracted intensity as a function of the number of antennas N_a . In blue-green is the obtained result, and in orange is the theoretical dependency. The x axis represents which waveguide is considered (i.e., the number of antennas), and the y axis represents the normalized intensity.

of the injection in the waveguide, as well as the overall quality of the waveguide itself and of the antennas. In order to try and determine if the antennas were impacting the overall flux propagating inside the waveguide, the outputs of each of the waveguides were also imaged, and the intensities at these outputs were measured. It was found that there is no significant intensity difference in the modal profiles at the outputs of the waveguides, meaning that the antennas are not perturbing the flux propagating in the waveguide, at least within the precision of our bench. This implies that the number of antennas can be increased without inducing notable flux losses in the waveguide.

IV. CONCLUSION

The building blocks developed in this work show promising results for the implementation of a fully direct laser written SWIFTS spectrometer in the mid-infrared. We obtained functional mid-IR waveguides with a satisfying absorption coefficient compared to literature values; the grooves that were etched extracted the light as expected, and we were allowed to sample an interferogram obtained through external modulation. The extracted flux varies linearly with the number of antennas, and this number does not noticeably impact the light propagating in the waveguide, meaning that the number of antennas can still be increased (so as to increase the resolution).

In order to improve these results, several steps can be taken. The first one is to try to obtain a reconstructed spectrum using the sample with 41 antennas in a Gabor configuration with an external modulation. Additionally, newer technological runs would allow to slightly reduce the crown size of the waveguide so as to ensure a single-mode guiding (a crown size of 30 μm has already been implemented with similar parameters and would lead to a single-mode waveguide in the wavelength of interest). As can be observed in Fig. 5, the grooves, even cleaned, are still rather rugged, and an additional smoothing step (thermal treatment of the sample) could help in reducing the roughness of the grooves as well as improve the propagation losses.³⁴ Finally, a new technological run to optimize the electrode deposition onto the sample will allow for the implementation of the electro-optic effect and modulate the phase of the fringes in the interferogram thanks to the Pockels effect shown by lithium niobate.

Such a spectrometer would show interesting characteristics: in both the passive and active design, the measurement time required by a SWIFTS to obtain a spectrum is limited by the detector's frame rate. In a passive design, it is instantaneous, as all the sampling points are obtained simultaneously, but the sampling is limited by the pixel pitch of the detector, therefore reducing the spectral bandwidth. An active design will allow to increase the spectral bandwidth but will require a higher measurement time: the electro-optic effect can be considered instantaneous, but the detector frame rate will limit the modulation frequency that can be used to scan the fringes. Furthermore, the chip on which the photonic functions are implemented is not strongly temperature sensitive, and the electro-optic effect is effective over a large temperature range (commercial electro-optic modulators are working in a large temperature range, from 0 to 70 °C for instance). This implies that even if the injection module or the detector require to be cooled down (which is eased in the case of a miniature spectrometer), it will not impact the performance of the device.

ACKNOWLEDGMENTS

IPAG funding: The authors acknowledge the funding from Labex FOCUS (Grant No. ANR-11-LABX-0013) and ASHRA (Action Spécifique Haute Résolution Angulaire) from INSU-CNRS.

USAL funding: We acknowledge support from the Ministerio de Ciencia e Innovación (Grant Nos. PID2020-119818 GB and PID2023-149836NB).

AUTHOR DECLARATIONS

Conflict of Interest

The authors have no conflicts to disclose.

Author Contributions

Myriam Bonduelle: Writing – original draft (lead). **Guillermo Martin:** Writing – original draft (equal). **Alain Morand:** Writing – original draft (equal). **Javier R. Vázquez de Aldana:** Writing – original draft (equal). **Víctor Arroyo Heras:** Writing –

original draft (supporting). **Carolina Romero:** Writing – original draft (supporting).

DATA AVAILABILITY

The data that support the findings of this study are available from the corresponding author upon reasonable request.

REFERENCES

- R. J. Dorn, P. Bristow, J. V. Smoker, F. Rodler, A. Lavail, M. Accardo, M. van den Ancker, D. Baade, A. Baruffolo, B. Courtney-Barrer, L. Blanco, A. Brucalassi, C. Cumani, R. Follert, A. Haimerl, A. Hatzes, M. Haug, U. Heiter, R. Hinterschuster, N. Hubin, D. J. Ives, Y. Jung, M. Jones, H. U. Kaeuffl, J. P. Kirchbauer, B. Klein, O. Kochukhov, H. H. Korhonen, J. Köhler, J. L. Lizon, C. Moins, I. Molina-Conde, T. Marquart, M. Neeser, E. Oliva, L. Pallanca, L. Pasquini, J. Paufigue, N. Piskunov, A. Reiners, D. Schneller, R. Schmutzer, U. Seemann, D. Slumstrup, A. Smette, J. Stegmeier, E. Stempels, S. Tordo, E. Valenti, J. J. Valenzuela, J. Vernet, J. Vinther, and A. Wehrhahn, "CRIRES⁺ on sky at the ESO Very Large Telescope. Observing the Universe at infrared wavelengths and high spectral resolution," *Astron. Astrophys.* **671**, A24 (2023).
- Z. Han, P. Lin, V. Singh, L. Kimerling, J. Hu, K. Richardson, A. Agarwal, and D. T. H. Tan, "On-chip mid-infrared gas detection using chalcogenide glass waveguide," *Appl. Phys. Lett.* **108**, 141106 (2016).
- K. B. Beć, J. Grabska, and C. W. Huck, "Near-infrared spectroscopy in bio-applications," *Molecules* **25**, 2948 (2020).
- M. D. Mengin Fondragon, "Etude d'un spectromètre intégré SWIFTS pour réaliser des capteurs optiques fibrés pour les sciences de l'observation," Ph.D. thesis, Université de Grenoble, 2014.
- H. Sun, Y. Zhou, and L. Li, "Miniature integrated spectrometers towards high-performance and cost-effective," *Light: Sci. Appl.* **12**, 259 (2023).
- Z. Yang, T. Albrow-Owen, H. Cui, J. Alexander-Webber, F. Gu, X. Wang, T.-C. Wu, M. Zhuge, C. Williams, P. Wang, A. V. Zayats, W. Cai, L. Dai, S. Hofmann, M. Overend, L. Tong, Q. Yang, Z. Sun, and T. Hasan, "Single-nanowire spectrometers," *Science* **365**, 1017–1020 (2019).
- L. Guo, H. Sun, M. Wang, M. Wang, L. Min, F. Cao, W. Tian, and L. Li, "A single-dot perovskite spectrometer," *Adv. Mater.* **34**, 2200221 (2022).
- H. H. Yoon, H. Fernandez, F. Nigmatulin, W. Cai, Z. Yang, H. Cui, F. Ahmed, X. Cui, G. Uddin, E. Minot, H. Lipsanen, K. Kim, P. Hakonen, T. Hasan, and Z. Sun, "Miniaturized spectrometers with a tunable van der Waals junction," *Science* **378**, 296–299 (2022).
- A. Li, C. Yao, J. Xia, H. Wang, Q. Cheng, R. Penty, Y. Fainman, and S. Pan, "Advances in cost-effective integrated spectrometers," *Light: Sci. Appl.* **11**, 174 (2022).
- M. Muneeb, X. Chen, P. Verheyen, G. Lepage, S. Pathak, E. Ryckeboer, A. Malik, B. Kuyken, M. Nedeljkovic, J. Van Campenhout, G. Mashanovich, and G. Roelkens, "Demonstration of silicon-on-insulator mid-infrared spectrometers operating at 38 μm ," *Opt. Express* **21**, 11659–11669 (2013).
- S. Yuan, D. Naveh, K. Watanabe, T. Taniguchi, and F. Xia, "A wavelength-scale black phosphorus spectrometer," *Nat. Photonics* **15**, 601–607 (2021).
- Q. Qiao, X. Liu, Z. Ren, B. Dong, J. Xia, H. Sun, C. Lee, and G. Zhou, "MEMS-enabled on-chip computational mid-infrared spectrometer using silicon photonics," *ACS Photonics* **9**, 2367 (2022).
- Z. Yang, T. Albrow-Owen, W. Cai, and T. Hasan, "Miniaturization of optical spectrometers," *Science* **371**, eabe0722 (2021).
- C. M. Simonescu, "Application of FTIR spectroscopy in environmental studies," in *Advanced Aspects of Spectroscopy*, edited by M. A. Farrukh (IntechOpen, Rijeka, 2012), Chap. 2.
- L. Mostaço-Guidolin and L. Bachmann, "Application of FTIR spectroscopy for identification of blood and leukemia biomarkers: A review over the past 15 years," *Appl. Spectrosc. Rev.* **46**, 388–404 (2011).

- ¹⁶S. Zheng, J. Zou, H. Cai, J. Song, L. Chin, P. Liu, Z. Lin, D. Kwong, and A.-Q. Liu, "Microring resonator-assisted Fourier transform spectrometer with enhanced resolution and large bandwidth in single chip solution," *Nat. Commun.* **10**, 2349 (2019).
- ¹⁷A. Li and Y. Fainman, "Integrated silicon Fourier transform spectrometer with broad bandwidth and ultra-high resolution," *Laser Photonics Rev.* **15**, 2000358 (2021).
- ¹⁸E. Le Coarer, S. Blaize, P. Benech, I. Stefanon, A. Morand, G. Lérondel, G. Leblond, P. Kern, J. M. Fedeli, and P. Royer, "Wavelength-scale stationary-wave integrated Fourier-transform spectrometry," *Nat. Photonics* **1**, 473–478 (2007); [arXiv:0708.0272](https://arxiv.org/abs/0708.0272) [physics.optics].
- ¹⁹J. Ferrand, G. Custillon, G. Leblond, F. Thomas, T. Moulin, E. Le Coarer, A. Morand, S. Blaize, T. Gonthiez, and P. Benech, "Stationary wave integrated Fourier transform spectrometer (SWIFTS)," *Proc. SPIE* **7604**, 760414 (2010).
- ²⁰S. Heidmann, "Composants actifs en optique intégrée pour l'interférométrie stellaire dans le moyen infrarouge," Ph.D. thesis, Université de Grenoble, 2013.
- ²¹D. Pohl, M. Reig Escalé, M. Madi, F. Kaufmann, P. Brotzer, A. Sergeev, B. Guldemann, P. Giaccari, E. Alberti, U. Meier, and R. Grange, "An integrated broadband spectrometer on thin-film lithium niobate," *Nat. Photonics* **14**, 24–29 (2020).
- ²²G. Finco, G. Li, D. Pohl, M. Reig Escalé, A. Maeder, F. Kaufmann, and R. Grange, "Monolithic thin-film lithium niobate broadband spectrometer with one nanometre resolution," *Nat. Commun.* **15**, 2330 (2024).
- ²³A. Morand, I. Heras, G. Ulliac, E. Le Coarer, P. Benech, N. Courjal, and G. Martin, "Improving the vertical radiation pattern issued from multiple nanogroove scattering centers acting as an antenna for future integrated optics Fourier transform spectrometers in the near IR," *Opt. Lett.* **44**, 542–545 (2019).
- ²⁴M. Bonduelle, I. Heras, A. Morand, G. Ulliac, R. Salut, N. Courjal, and G. Martin, "Near IR stationary wave Fourier transform lambda meter in lithium niobate: Multiplexing and improving optical sampling using spatially shifted nanogroove antenna," *Appl. Opt.* **60**, D83–D92 (2021).
- ²⁵M. Leidinger, S. Fieberg, N. Waasem, F. Kühnemann, K. Buse, and I. Breunig, "Comparative study on three highly sensitive absorption measurement techniques characterizing lithium niobate over its entire transparent spectral range," *Opt. Express* **23**, 21690–21705 (2015).
- ²⁶M. Heinrich, K. Rademaker, and S. Nolte, "Waveguides in crystalline materials," in *Femtosecond Laser Micromachining: Photonic and Microfluidic Devices in Transparent Materials*, edited by R. Osellame, G. Cerullo, and R. Ramponi (Springer, Berlin, Heidelberg, 2012), pp. 295–313.
- ²⁷C. Phipps, *Laser Ablation and Its Applications*, 129 (Springer, 2007).
- ²⁸R. Gattass and E. Mazur, "Femtosecond laser micromachining in transparent materials," *Nat. Photonics* **2**, 219–225 (2008).
- ²⁹K. M. Davis, K. Miura, N. Sugimoto, and K. Hirao, "Writing waveguides in glass with a femtosecond laser," *Opt. Lett.* **21**, 1729–1731 (1996).
- ³⁰R. R. Thomson, S. Campbell, I. J. Blewett, A. K. Kar, and D. T. Reid, "Optical waveguide fabrication in z-cut lithium niobate (LiNbO₃) using femtosecond pulses in the low repetition rate regime," *Appl. Phys. Lett.* **88**, 111109 (2006).
- ³¹L. Li, W. Kong, and F. Chen, "Femtosecond laser-inscribed optical waveguides in dielectric crystals: A concise review and recent advances," *Adv. Photonics* **4**, 024002 (2022).
- ³²A. G. Okhrimchuk, A. V. Shestakov, I. Khrushchev, and J. Mitchell, "Depressed cladding, buried waveguide laser formed in a YAG:Nd³⁺ crystal by femtosecond laser writing," *Opt. Lett.* **30**, 2248–2250 (2005).
- ³³H. Karakuzu, M. Dubov, and S. Boscolo, "Control of the properties of microstructured waveguides in lithium niobate crystal," *Opt. Express* **21**, 17122–17130 (2013).
- ³⁴H.-D. Nguyen, A. Ródenas, J. R. V. de Aldana, G. Martín, J. Martínez, M. Aguiló, M. C. Pujol, and F. Díaz, "Low-loss 3D-laser-written mid-infrared LiNbO₃ depressed-index cladding waveguides for both TE and TM polarizations," *Opt. Express* **25**, 3722–3736 (2017).
- ³⁵H. Nguyen, "Three-dimensional laser writing of mid-infrared waveguides circuits in lithium niobate crystal," Ph.D. thesis, Universitat Rovira i Virgili, 2017.
- ³⁶This colormap and others come from the CMasher catalog.³⁷
- ³⁷E. van der Velden, "CMasher: Scientific colormaps for making accessible, informative and 'cmashing' plots," *J. Open Source Softw.* **5**, 2004 (2020).